2026 IEEE International Conference on Robotics and Automation (ICRA 2026)
June 1-5, 2026. Vienna, Austria

# A Dual–Field Framework for Urban Low–Altitude UAV Traffic Planning and Management

Zhaoqi Dong[1], and Lei Chen[2]

*Abstract*— **Urban Air Mobility emerges as a transformative mode of transportation, but its integration into complex low–altitude urban environments requires systematic consideration of safety and efficiency. This study aims to develop a computational framework that enables structured traffic organization while accounting for spatially variant risks. The framework introduces a dual–field environmental model that couples a traversability field, which quantifies continuous anisotropic risk, with a scalar potential field, which encodes macroscopic traffic flow. The path planning formulation computes geodesics under an anisotropic metric derived from the dual–field, and the centralized coordination mechanism updates the fields to maintain real–time deconfliction. Simulation results demonstrate that the proposed framework generates paths that reduce exposure to high–risk regions to a negligible level and achieve a substantial reduction in average curvature compared to a baseline planner. Furthermore, the local update mechanism provides significant computational speedup for dynamic real–time scenarios. These results validate the capability of the dual–field framework to unify safety and efficiency in urban airspace management, providing a scalable foundation for future unmanned traffic management systems.**

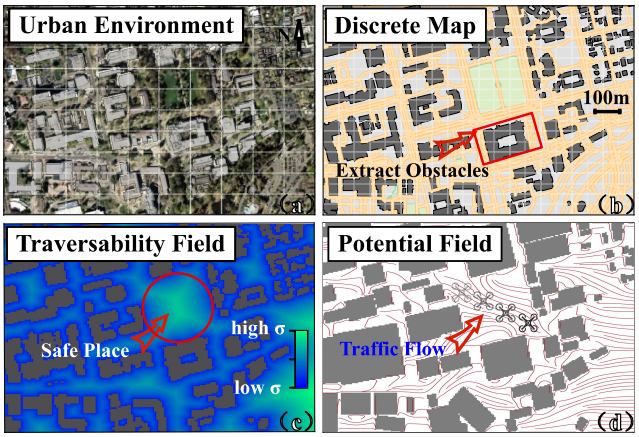


Fig. 1: An illustration of the dual–field modeling process, transforming a real–world urban environment (a, b) into a coupled representation of a traversability field ($\sigma$) for risk and a potential field ($\psi$) for macroscopic traffic flow (c, d).

## I. INTRODUCTION

The advancement of Urban Air Mobility [1], [2] and Unmanned Aerial Vehicle (UAV) technologies [3], [4] signals a transformative shift in urban transportation and services. These technologies unlock potential in diverse applications, such as autonomous logistics [5], public safety operations [6], and critical infrastructure monitoring [7]. The integration of these vehicles into urban airspace promises to improve operational efficiency and create new economic opportunities.

The safe integration of these aerial vehicles into urban airspace, however, hinges on addressing the challenges of navigating complex and dynamic low-altitude environments [8]. A core challenge lies in establishing an operational framework that defines safe, efficient, and predictable flight paths, moving beyond simple obstacle avoidance [9]. This necessity motivates the development of a sophisticated Unmanned Traffic Management (UTM) system [10]. Such a system must provide a framework for managing airspace access, deconflicting operations [11], and structuring overall traffic flow. In pursuit of a structured traffic flow, a primary strategy involves Air Traffic Flow Management [11]–[13], which seeks to balance traffic demand against airspace capacity. This approach relies on large–scale optimization methods [12], [13] to schedule aerial vehicle trajectories and mitigate system–wide congestion and delays. A fundamental limitation of this management paradigm, however, is its presupposition of a well–defined navigable airspace structure, a condition precisely lacking in complex urban environments. Physics–inspired models address this gap by imposing macroscopic order on traffic. Flow–field approaches create corridor–like guidance and streamline families around fixed obstacles and provide a predictable global organization [14], [15]. Fixed–corridor formulations further partition airspace into altitude layers and prescribe streamline-aligned motion, producing repeatable structure in cluttered scenes [16].

While these physics–inspired frameworks succeed in defining a macroscopic traffic organization, their effectiveness is limited at the trajectory level because they rely on overly simplistic cost metrics for their underlying path planners. These metrics are typically isotropic, meaning that the cost of movement is treated as uniform in all directions and is primarily dependent on the geometric distance [17]. A fundamental conflict thus arises, since these systems attempt to impose a directional traffic structure, a behavior that requires an anisotropic representation where cost is directionally dependent, while the planners operating within them make decisions based on these simple and isotropic costs. This disconnect can lead to trajectories that are locally optimal with respect to distance but globally suboptimal, as they may ignore the intended flow direction or traverse areas

This work was supported in part by the National Natural Science Foundation of China under Grants 62088101 and 62003015.

[1]Zhaoqi Dong is with the Advanced Research Institute of Multidisciplinary Sciences and State Key Laboratory of CNS/ATM, Beijing Institute of Technology, Beijing 100081, China. dongzhaoqi@bit.edu.cn

[2]Lei Chen is with the School of Artificial Intelligence, Beijing Institute of Technology, Beijing 100081, China. bit_chen@bit.edu.cn

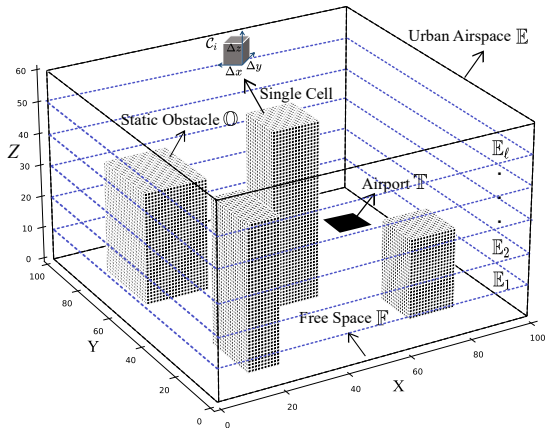


Fig. 2: Discretized representation of the bounded urban airspace $\mathbb{E}$, including obstacle region $\mathbb{O}$, navigable free space $\mathbb{F}$, and designated take–off and landing sites $\mathbb{T}$.

of unmodeled and spatially variant risk [18]. This reveals a critical need for a computational framework that provides an anisotropic representation, unifying both macroscopic directional flow and spatially variant risk, enabling the generation of paths that are jointly optimized for safety.

To address this need, this paper proposes a dual–field environmental modeling framework to represent and manage low–altitude urban airspace with anisotropic properties, as illustrated in Fig. 1. The framework consists of two coupled components: a traversability field and a scalar potential field. The traversability field quantifies a continuous, spatially variant risk profile. The potential field establishes macroscopic traffic flows throughout the airspace. The main contributions are summarized as follows:

1) This work introduces a dual–field framework based on an anisotropic elliptic PDE, which integrates macroscopic traffic flow and spatially variant environmental risk into a unified computational model.
2) The path planning problem is formulated as a geodesic search guided by an anisotropic metric derived from the dual–fields, generating trajectories that follow traffic flow while avoiding high–risk regions.
3) The centralized traffic coordination mechanism applies local updates to the dual–field model, enabling efficient real–time deconfliction while reducing the computational load compared with global re–computation.

The remainder of this paper is organized as follows. Section II establishes the representation of the urban airspace with discretization, obstacles, and flight levels. Section III presents the dual–field framework, the geodesic path planning, and the centralized coordination mechanism. Section IV evaluates the framework through field analysis, ablation, and dynamic deconfliction experiments in a simulated urban environment. Section V summarizes the findings and outlines directions for future work.

## II. Urban Environment Modeling

The bounded airspace is defined as $\mathbb{E} \subset \mathbb{R}^3$ in a global Cartesian coordinate system $(x, y, z)$, covering the horizontal range $[x_{\min}, x_{\max}] \times [y_{\min}, y_{\max}]$ and the altitude range $[z_{\min}, z_{\max}]$. The domain is uniformly discretized into cuboidal cells with resolutions $(\Delta x, \Delta y, \Delta z)$, yielding a finite set $\mathbb{C} = \{\mathcal{C}_i \mid i = 1, \ldots, N\}$ that partitions the environment without overlap, as illustrated in Fig. 2.

Static obstacles are represented by a subset $\mathbb{O} \subset \mathbb{E}$, and the remaining region constitutes the free space $\mathbb{F} = \mathbb{E} \setminus \mathbb{O}$. Within the free space, a finite set of take–off and landing sites $\mathbb{T} = \{a_j \mid j = 1, \ldots, M\}$ is defined, where each site $a_j$ corresponds to the center of a free cell and serves as an access point for UAV operations.

The vertical structure of the airspace is divided into $H$ discrete flight levels. The $\ell$-th level is denoted by

$$\mathbb{E}_\ell = \{(x, y, z) \in \mathbb{E} \mid z_\ell \leqslant z < z_{\ell+1}\}, \tag{1}$$

where $z_\ell = z_{\min} + (\ell - 1)\Delta z$. At each level, the free region and obstacle region are expressed as $\mathbb{F}_\ell = \mathbb{E}_\ell \setminus \mathbb{O}$ and $\mathbb{O}_\ell = \mathbb{E}_\ell \cap \mathbb{O}$, respectively. Let $N_\ell$ denote the number of discrete grid nodes contained in $\mathbb{F}_\ell$.

## III. METHOD

### A. Dual–Field Environmental Modeling

The dual–field framework models each flight level $\mathbb{E}_\ell \subset \mathbb{R}^2$ of the navigable airspace through an anisotropic elliptic equation. The scalar potential field $\psi_\ell : \mathbb{E}_\ell \times \mathbb{R}^+ \to \mathbb{R}$ encodes the organization of the macroscopic flow within the level $\ell$, and the traversability field $\sigma_\ell : \mathbb{E}_\ell \times \mathbb{R}^+ \to \mathbb{R}^+$ reflects the spatial variation of the risk. The interaction between $\psi_\ell$ and $\sigma_\ell$ is governed by

$$\nabla \cdot (\sigma_\ell(p, t)\nabla\psi_\ell(p, t)) = 0, \quad p \in \mathbb{E}_\ell, \tag{2}$$

where $\psi_\ell(p, t)$ denotes the scalar potential field whose gradient indicates the direction of the modeled traffic flow, $\sigma_\ell(p, t)$ is the spatially and temporally varying traversability function, and $\nabla$ and $\nabla\cdot$ denote the gradient and divergence operators, respectively. For any given traversability field $\sigma_\ell(p, t)$ at a specific time $t$, the potential field $\psi_\ell(p, t)$ is assumed to reach an instantaneous equilibrium.

The traversability field $\sigma_\ell(p, t)$ combines local and global risk components through

$$\sigma_\ell(p, t) = \sigma_{1,\ell}(p, t)\sigma_{2,\ell}(p, t), \tag{3}$$

where $\sigma_{1,\ell}(p, t)$ quantifies the local traversability based on proximity to obstacles within level $\ell$, and $\sigma_{2,\ell}(p, t)$ introduces global modulation based on obstacle density in that level. The function $\sigma_{1,\ell}(p, t)$ increases with the Euclidean distance to the nearest obstacle boundary. Let $d_\ell(p) = \inf_{q \in \partial(\mathbb{O} \cap \mathbb{E}_\ell)} \|p - q\|_2$ denote the minimal distance from the point $p$ to the boundary of the obstacle region at level $\ell$. The local traversability component is defined as follows:

$$\sigma_{1,\ell}(p, t) = \sigma_{\min} + (\sigma_{\max} - \sigma_{\min}) \left(1 - e^{-d_\ell(p)/k}\right), \tag{4}$$

where $\sigma_{\min}, \sigma_{\max} > 0$ define the lower and upper limits of traversability and $k > 0$ is a scaling factor that controls the steepness of the traversability gradient near obstacles. The global modulation component $\sigma_{2,\ell}(p,t)$ maps each spatial location $p \in \mathbb{E}_\ell$ and time $t$ to a weight based on the density of the obstacle at the level $\ell$. The normalized obstacle density for level $\ell$ is given by

$$\rho(\mathbb{E}_\ell) = \frac{\mu(\mathbb{O} \cap \mathbb{E}_\ell)}{\mu(\mathbb{E}_\ell)}, \tag{5}$$

where $\mu(\cdot)$ denotes the two–dimensional Lebesgue measure and $\rho(\mathbb{E}_\ell)$ represents the proportion of the area occupied by obstacles. The modulation function is given as follows:

$$\sigma_{2,\ell}(p,t) \;=\; \max\left\{\varepsilon,\; \big(1-\rho(\mathbb{E}_\ell)\big)^{\beta}\right\}, \varepsilon \in (0, \sigma_{\min}), \tag{6}$$

where $\beta > 0$ controls the decay rate near the threshold, and the positive lower bound $\varepsilon$ prevents degeneracy. Since $\sigma_{1,\ell} \in [\sigma_{\min}, \sigma_{\max}]$ and $\sigma_{2,\ell} \geq \varepsilon$, the composite traversability satisfies $0 < \varepsilon\,\sigma_{\min} \leq \sigma_\ell(p,t) \leq \sigma_{\max}$, which preserves the uniform ellipticity of Eq.(2).

The domain $\mathbb{E}_\ell$ uses the uniform Cartesian grid to discretize with nodes $p_{i,j}$ and spacings $\Delta x, \Delta y$. A finite difference scheme approximates the divergence term in Eq. (2). To preserve stencil symmetry and ensure normal–flux continuity, we evaluates the traversability $\sigma_\ell$ at the face center $p_{i+\frac{1}{2},j}$ using a harmonic mean through

$$\sigma_\ell(p_{i+\frac{1}{2},j}, t) = \frac{2\,\sigma_\ell(p_{i+1,j},t)\,\sigma_\ell(p_{i,j},t)}{\sigma_\ell(p_{i+1,j},t) + \sigma_\ell(p_{i,j},t)}, \tag{7}$$

where $p_{i+\frac{1}{2},j}$ is the face center between nodes $p_{i,j}$ and $p_{i+1,j}$. The discretization yields a sparse linear system for each flight level, expressed as

$$\mathbf{A}_\ell(t)\,\boldsymbol{\psi}_\ell(t) = \mathbf{b}_\ell(t), \tag{8}$$

where $\mathbf{A}_\ell(t) \in \mathbb{R}^{N_\ell \times N_\ell}$ is the sparse coefficient matrix generated from the traversability field at time $t$, $\boldsymbol{\psi}_\ell(t) \in \mathbb{R}^{N_\ell}$ is the discrete vector of potential values at all grid nodes of level $\ell$, and $\mathbf{b}_\ell(t) \in \mathbb{R}^{N_\ell}$ is the vector determined by the boundary conditions. A set of mixed Dirichlet and Neumann boundary conditions is imposed on the perimeter $\partial\mathbb{E}_\ell$ to model the traffic flow. The primary potential gradient is established by Dirichlet conditions on the inflow and outflow boundaries through

$$\psi_\ell(p,t) = 1, \quad \forall p \in \partial\mathbb{E}_{\ell,\text{in}}, \tag{9}$$

$$\psi_\ell(p,t) = 0, \quad \forall p \in \partial\mathbb{E}_{\ell,\text{out}}. \tag{10}$$

Homogeneous Neumann conditions on the lateral boundaries define no–flux surfaces through

$$\frac{\partial\psi_\ell}{\partial\mathbf{n}}(p,t) = 0, \quad \forall p \in \partial\mathbb{E}_{\ell,\text{lateral}}, \tag{11}$$

where $n$ is the normal vector to the boundary. The no–flux condition at obstacle perimeters is enforced numerically during discretization. For any grid node $p$ that falls within an obstacle region $\mathbb{O}\cap\mathbb{E}_\ell$, the traversability value is $\sigma_\ell(p,t) = \varepsilon$. This high resistance to flow effectively makes obstacles impenetrable in the model. The solution of the linear system in Eq. (8) yields the discrete potential field $\boldsymbol{\psi}_\ell$.

### *B. Path Planning as Geodesic Computation*

This work formulates the path planning problem for the UAV $j$, as finding a geodesic on a discretized manifold. This manifold is represented by a 3D grid graph $\mathbb{G} = (\mathbb{V}, \mathbb{N})$. The vertex set $\mathbb{V}$ consists of the center points of all non–obstacle cells in the free space $\mathbb{F}$. The edge set $\mathbb{N}$ connects adjacent vertices with 8–connectivity on horizontal planes and with direct links between designated flight levels.

The geodesic path is obtained using the A* search algorithm with a cost function $f(n) = g(n)+h(n)$. The heuristic $h(n)$ is required to be admissible to preserve optimality, which means that it provides a lower bound on the true remaining cost. In the proposed anisotropic metric space, the Euclidean distance does not satisfy this requirement because edge costs are modulated by the traversability field and the flow guidance function. Therefore, we define an admissible heuristic by scaling the Euclidean distance with the minimum possible cost per unit distance in the entire domain through

$$h(n) = l_{\min} \cdot \|p_g - p_n\|_2, \tag{12}$$

where $l_{\min} = \min(1/\sigma_{\max}, w_z)$ is a lower bound on the cost to traverse a unit distance, derived from the maximum possible traversability $\sigma_{\max}$ for horizontal movement and the vertical cost coefficient $w_z$. This construction guarantees that $h(n)$ is a consistent and admissible heuristic, thus preserving the optimality of the A* search.

The cost accumulated from the start node $s$, $g(n)$ is the sum of the edge traversal costs. If the path to a node $n$ is the sequence of vertices $(v_0, v_1, \ldots, v_k)$, where $v_0 = s$ and $v_k = n$, then $g(n)$ is defined as

$$g(n) = \sum_{i=0}^{k-1} c(v_i, v_{i+1}), \tag{13}$$

with the base case $g(s) = 0$. The edge traversal cost $c(u,v)$ defines an anisotropic metric in the manifold and is given by a unified piecewise function. Let $z(v)$ be the flight level of a vertex $v$. The cost is given by

$$c(u,v) = \begin{cases} \dfrac{\|p_v - p_u\|_2}{\sigma_{\text{avg}}}\mathcal{A}(u,v), & \text{if } z(u) = z(v) \\ w_z\|p_v - p_u\|_2, & \text{if } z(u) \neq z(v) \end{cases} \tag{14}$$

For horizontal movement ($z(u) = z(v)$), the cost is based on average traversability $\sigma_{\text{avg}} = \frac{1}{2}(\sigma_\ell(p_u) + \sigma_\ell(p_v))$ and an anisotropic guidance function $\mathcal{A}(u,v)$. This function penalizes deviations from the ideal flow direction given by the potential field and is defined as

$$\mathcal{A}(u,v) = 1 + \alpha\left(1 - \frac{(p_v - p_u)\cdot(-\nabla\psi_\ell(p_u))}{\|p_v - p_u\|_2\| - \nabla\psi_\ell(p_u)\|_2}\right), \tag{15}$$

where $\alpha$ is the guide weight. For vertical movement ($z(u) \neq z(v)$), the cost is proportional to the Euclidean distance, scaled by the coefficient $w_z$.

A second–order central difference scheme approximates the gradient of the potential field at a vertex $p_{i,j}$ through

$$\nabla\psi_\ell(p_{i,j}) \approx \left(\frac{\psi_{i+1,j} - \psi_{i-1,j}}{2\Delta x}, \frac{\psi_{i,j+1} - \psi_{i,j-1}}{2\Delta y}\right), \tag{16}$$

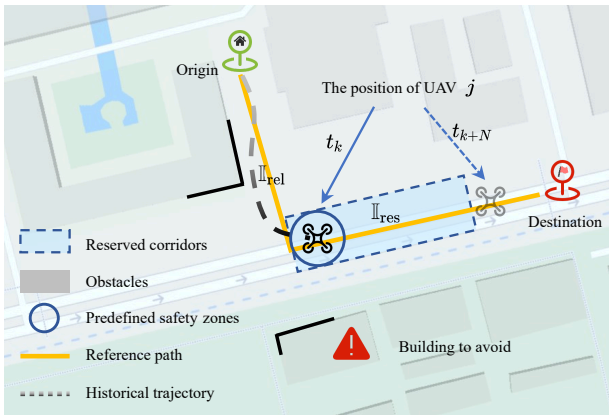


Fig. 3: The centralized coordination cycle registers UAV planned 4D corridor $\mathbb{I}_j(t_k)$ along trajectory $\gamma_j(t)$, reserves new segments $\mathbb{I}_{\text{res}}$ and releases traversed segments $\mathbb{I}_{\text{rel}}$.

where $\psi_{i,j}$ is the potential value at the vertex $p_{i,j}$ and $\Delta x, \Delta y$ are the grid spacings. At the boundaries of the domain, where a full central difference stencil is unavailable, the gradient is approximated using a first-order forward or backward difference scheme. This cost formulation yields a path that is a discrete geodesic in the metric space induced by the dual–field model.

### C. Centralized Traffic Coordination

The centralized UTM system coordinates all flight operations by maintaining a unified, time–varying master dual–field that represents the current state of the entire 3D airspace. For the purpose of centralized coordination and dynamic updates, the set of fields per level $\{(\psi_\ell, \sigma_\ell)\}$ described previously are assembled into a single 3D field representation. The 3D traversability at any point $p \in \mathbb{R}^3$ is given by the traversability of the flight level $\mathbb{E}_\ell$ to which $p$ belongs. The system completes air traffic management through a recurrent "plan–reserve–update–release" cycle in this unified 3D field.

The cycle initiates upon a flight request from a UAV $j$, at time $t_k$. Its planned 4D trajectory is then registered as a reserved space–time corridor, defined as a set in $\mathbb{R}^3 \times \mathbb{R}^+$

$$\mathbb{I}_j(t_k) = \{(p,t) \mid t_k \leqslant t \leqslant t_{k+N}, \|p - \gamma_j(t)\|_2 \leqslant r_s\}, \quad (17)$$

where $\gamma_j(t) : \mathbb{R}^+ \to \mathbb{R}^3$ is the continuous 3D path of the UAV $j$, $t_{k+N} - t_k$ is the reservation time horizon, and $r_s$ is a predefined safety radius. The reservation of new corridors and the release of traversed corridors trigger an update of the master dual–field from time $t_k$ to $t_{k+1}$, as shown in Fig. 3. The 3D traversability field $\sigma(p, t_{k+1})$ is updated from $\sigma(p, t_k)$ through the piecewise function

$$\sigma(p,t_{k+1}) = \begin{cases} \varepsilon, & \text{if } (p,t_{k+1}) \in \mathbb{I}_{\text{res}} \\ \sigma_{\text{bg}}(p), & \text{if } (p,t_{k+1}) \in \mathbb{I}_{\text{rel}} \\ \sigma(p,t_k), & \text{otherwise,} \end{cases} \quad (18)$$

where $\mathbb{I}_{\text{res}}$ is the set of all newly reserved corridors, and $\mathbb{I}_{\text{rel}}$ is the set of released corridors. The 3D background traversability $\sigma_{\text{bg}}(p)$ is constructed from the static, per–level fields, where for any $p \in \mathbb{E}_\ell$, $\sigma_{\text{bg}}(p) = \sigma_{1,\ell}(p', t_0) \cdot \sigma_{2,\ell}(p', t_0)$, with $p'$ being the 2D projection of $p$.

Subsequently, the 3D potential field $\psi(t_{k+1})$ is updated by solving a local 3D boundary value problem. The calculation is confined to a local update volume $\mathbb{M} \subset \mathbb{R}^3$, defined as a 3D boundary box that encloses all changed corridor segments ($\mathbb{I}_{\text{res}} \cup \mathbb{I}_{\text{rel}}$) plus a safety margin. The updated field is the solution to

$$\begin{cases} \nabla \cdot (\sigma(p,t_{k+1}) \nabla \psi(p,t_{k+1})) = 0, & \forall p \in \mathbb{M} \\ \psi(p,t_{k+1}) = \psi(p,t_k), & \forall p \in \partial\mathbb{M}, \end{cases} \quad (19)$$

where the Dirichlet boundary condition on the perimeter $\partial\mathbb{M}$ enforces value continuity with the surrounding, unchanged field, minimizing artifacts from the local update. This continuous reservation and release cycle ensures that any path computed on the master field is inherently deconflicted from all active reservations.

## IV. Simulation

### A. Experimental Setup

The simulation environment consists of a $100 \times 100 \times 70$ unit grid. To represent an urban setting, we randomly generate 20 rectangular obstacles with sizes ranging from $5 \times 5 \times 10$ to $15 \times 15 \times 65$ units. The navigable airspace is structured into six discrete flight levels, each assigned a macroscopic flow direction.

We define a comprehensive set of objective metrics to evaluate the quality of a path $\gamma = \{p_0, p_1, \ldots, p_N\}$. The length of the trajectory is measured as the total Euclidean distance $L(\gamma) = \sum \|p_{i+1} - p_i\|_2$, which reflects the overall efficiency of the path. To capture safety, integrated risk is introduced as $R_{int}(\gamma) = \sum(1 - \bar{\sigma}_i)\|p_{i+1} - p_i\|_2$, where $\bar{\sigma}_i$ denotes the average traversability along each segment, while the danger exposure quantifies the portion of the trajectory that enters regions with traversability $\sigma$ below a fixed threshold of 0.3. In addition to efficiency and safety, flight quality is assessed by average flow adherence, defined as the mean cosine similarity between each segment and the local potential gradient, which reflects compliance with macroscopic traffic conventions, and by the average curvature, computed as the mean angular change per unit distance at interior points, which measures the smoothness of the trajectory.

### B. Analysis of the Dual–Field Model

This section analyzes the properties of the proposed dual–field airspace model. The model is designed to generate a physics–informed representation of the airspace that encodes spatial risk through the traversability field and macroscopic traffic conventions through the potential field. Fig. 4 illustrates the resulting fields for all six navigable flight levels in the benchmark urban environment.

As shown in Fig. 4, the traversability field visualizes spatial risk through a background heatmap. The traversability is functionally dependent on the distance to the nearest obstacle (black squares), which creates a continuous risk gradient. The values are lowest within obstacle regions and

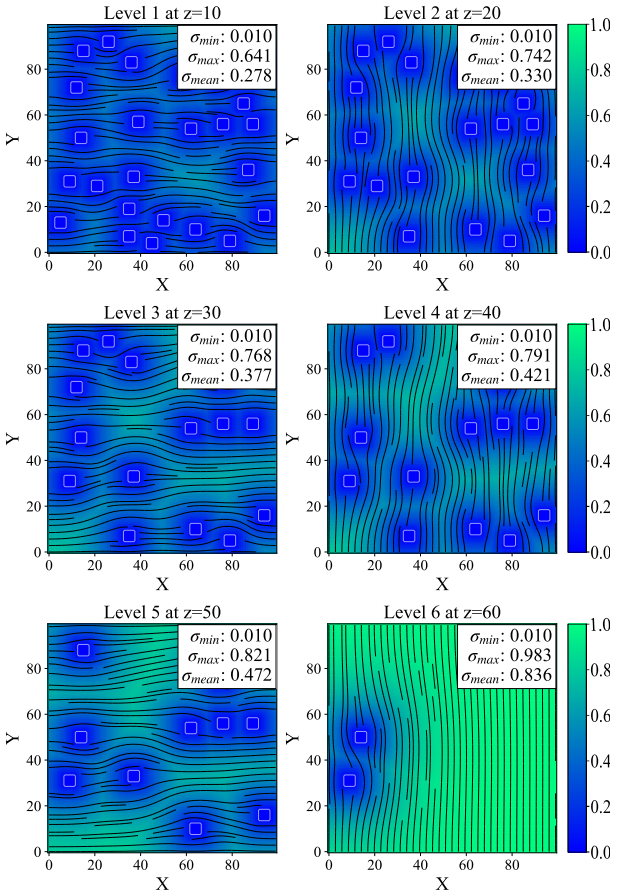


Fig. 4: The dual–field representation at multiple flight levels $\mathbb{E}_\ell$ illustrates the traversability field $\sigma_\ell$ that encodes spatial risk around obstacles $\mathbb{O}_\ell$ and the potential field $\psi_\ell$ that organizes macroscopic traffic flow in the free regions $\mathbb{F}_\ell$.

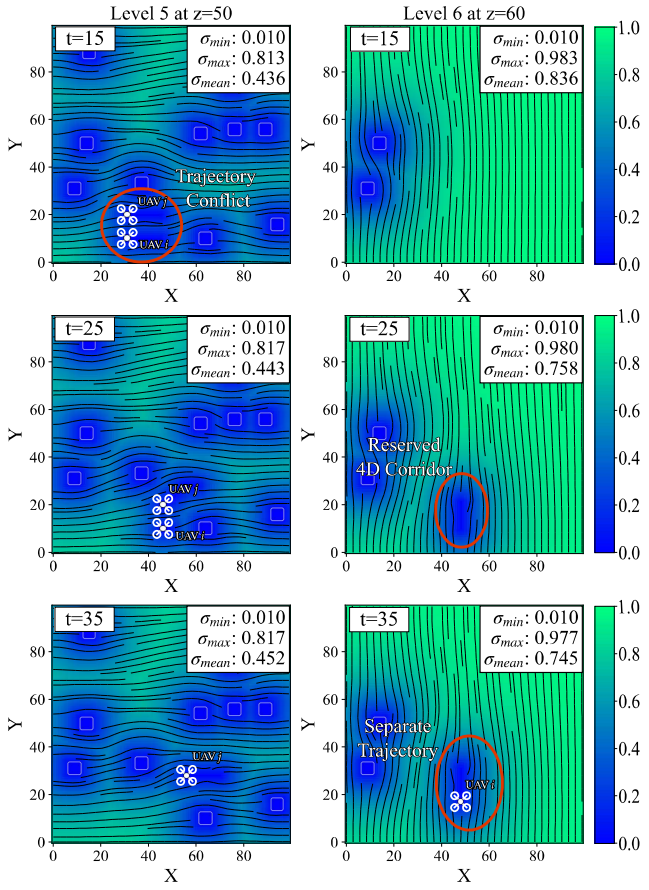


Fig. 5: The simulation illustrates the evolution of the traversability field $\sigma_\ell$ and the potential field $\psi_\ell$ at flight levels $\mathbb{E}_\ell$, where UAV trajectories $\gamma_j(t)$ initially conflict at level 5, then reserve a 4D corridor at level 6, and finally achieve separation into distinct trajectories under the dual–field coordination mechanism.

increase progressively in open airspace. This behavior is consistent at all altitudes, with quantitative data showing that the mean traversability increased from 0.28 at $z = 10$ to 0.84 at $z = 60$, reflecting the increase in the traversable area at higher altitudes with fewer obstacles.

The potential field establishes an orderly macroscopic traffic flow that smoothly circumnavigates the high-risk zones identified by the traversability field. The flow direction alternates between levels according to predefined conventions, and the streamlines become denser in narrow corridors, indicating a higher potential gradient. This analysis shows that the dual–field representation generates a structured environment with specific and measurable properties.

### C. Dynamic Traffic Deconfliction

The dynamic experiment evaluates both the effectiveness of the centralized management strategy and the efficiency of the field update mechanism. The experiment involves two UAVs that are initialized on trajectories with overlapping reserved space–time corridors, which creates a potential conflict as shown in Fig. 5.

The sequence in Fig. 5 describes the system response in three stages. In the initial stage at the flight level $z = 50$, the two UAVs follow intersecting trajectories that result in a potential conflict. In the second stage at the higher flight level $z = 60$, the centralized UTM system allocates a new four–dimensional corridor to UAV $i$ to separate the trajectories. In the final stage, UAV $i$ performs a vertical maneuver to the newly assigned level, while UAV $j$ continues at the original altitude without conflict. The sequence demonstrates how the framework manages traffic by reallocating airspace to maintain safe separation.

TABLE I: Comparison of computational performance

| Update Strategy | Computation Time (s) | Nodes Involved |
|---|---|---|
| Full Re–computation | 0.7093 | 54335 |
| Local Update | 0.1121 | 18585 |
| Relative Performance | 6.3x faster | 34.2% of baseline |

The efficiency of the deconfliction process depends on the performance of the field update mechanism. Each reservation or release of a corridor requires an update of the master field. To evaluate the computational cost, two strategies are com-

TABLE II: Quantitative results of the ablation study across 50 randomized urban environments

| Environment | Model | Path Length | Flow Adherence | Integrated Risk | Danger Exposure | Avg. Curvature |
|---|---|---|---|---|---|---|
| 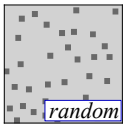  | Full Model | $235.3 \pm 12.4$ | $\mathbf{0.989 \pm 0.003}$ | $52.7 \pm 6.5$ | $\mathbf{0.00 \pm 0.00}$ | $\mathbf{0.018 \pm 0.03}$ |
| | No $\psi$–Guidance | $184.6 \pm 15.2$ | $0.807 \pm 0.120$ | $\mathbf{30.8 \pm 5.2}$ | $\mathbf{0.00 \pm 0.00}$ | $0.27 \pm 0.14$ |
| | No $\sigma$–Awareness | $231.1 \pm 14.8$ | $0.986 \pm 0.004$ | $119.2 \pm 10.3$ | $91.4 \pm 12.7$ | $0.024 \pm 0.03$ |
| | Baseline (A*) | $\mathbf{180.5 \pm 13.9}$ | $0.649 \pm 0.221$ | $116.0 \pm 9.8$ | $104.7 \pm 14.5$ | $0.43 \pm 0.18$ |
| 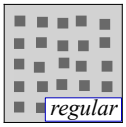  | Full Model | $219.8 \pm 12.6$ | $\mathbf{0.998 \pm 0.002}$ | $\mathbf{70.08 \pm 6.2}$ | $\mathbf{0.00 \pm 0.00}$ | $\mathbf{0.009 \pm 0.02}$ |
| | No $\psi$–Guidance | $176.5 \pm 14.2$ | $0.813 \pm 0.102$ | $94.9 \pm 7.4$ | $\mathbf{0.00 \pm 0.00}$ | $0.25 \pm 0.15$ |
| | No $\sigma$–Awareness | $219.2 \pm 13.7$ | $0.980 \pm 0.004$ | $128.29 \pm 9.5$ | $94.8 \pm 8.9$ | $0.012 \pm 0.02$ |
| | Baseline (A*) | $\mathbf{171.8 \pm 11.9}$ | $0.662 \pm 0.214$ | $106.72 \pm 8.1$ | $84.0 \pm 7.6$ | $0.22 \pm 0.13$ |

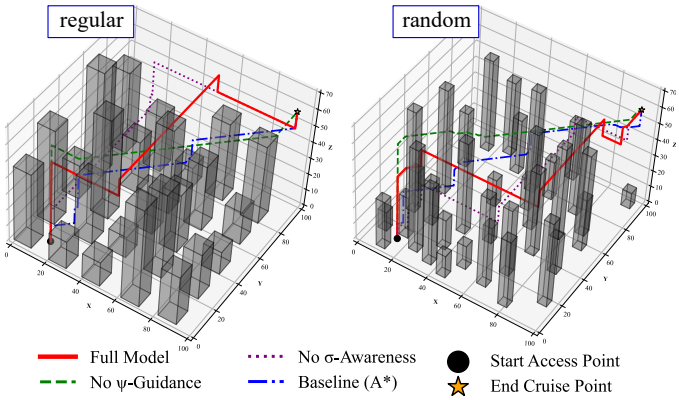


Fig. 6: Comparison of planned trajectories in two representative environments: a regular grid of aligned buildings (left) and a randomized urban layout (right).

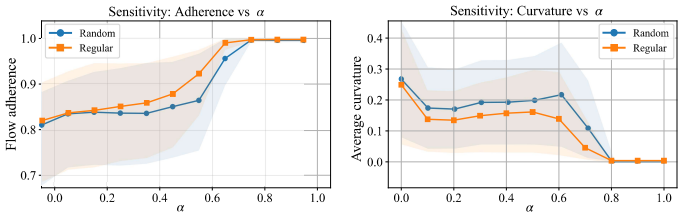


Fig. 7: Sensitivity analysis of the guidance weight $\alpha$, where flow adherence improves as $\alpha$ increases (left) and average curvature decreases (right), with shaded areas denoting the variance across 50 runs.

pared. Table I reports the results. The full re–computation strategy requires 0.7093 seconds for the initial solution and involves 54335 nodes in the update process. The local update strategy requires 0.1121 seconds after the introduction of a new no–fly zone and involves 18585 nodes. The results show that the local update executes about 6.3 times faster than the full re–computation and reduces the computational load to 34.2 percent of the baseline, which indicates its suitability for real–time dynamic airspace management.

### D. Ablation Study

To evaluate the contribution of each component of the proposed framework, we perform an ablation study by comparing the full model against three degraded variants: (i) no $\psi$–guidance, where the anisotropic guidance weight $\alpha$ is set to zero; (ii) no $\sigma$–awareness, where the traversability field is fixed to $\sigma = 1.0$; and (iii) a baseline A* search algorithm that ignores both fields. Fig. 6 presents representative trajectories in two environments. In the regular grid setting, the full model produces structured paths that closely follow the global flow while avoiding obstacles. In contrast, the no $\psi$–guidance variant yields feasible but irregular paths, while the no $\sigma$–awareness and baseline A* models cut directly through hazardous regions, compromising safety. In the randomized urban layout, the same trend persists: only the full model maintains both safety and global order.

The ablation study conducts over 50 independent experiments for each environment, fixing the UAV's takeoff and landing positions while randomly generating different city layouts. The results, summarized in Table II, show that the full model consistently guarantees safety with zero danger exposure across all runs, while also maintaining the highest flow adherence close to one and the lowest average curvature, thus producing safe and smooth trajectories. The variant without $\psi$–guidance remains safe in both environments, but its trajectories are less orderly and exhibit significantly larger curvature, particularly in the randomized layouts. In contrast, models without $\sigma$–awareness and the baseline A* frequently fail by traversing high-risk regions, resulting in integrated risk values well above one hundred and danger exposures exceeding 90, which confirms that safety cannot be ensured without the traversability field. The role of anisotropic guidance weight $\alpha$ is further illustrated in Fig. 7, where increasing $\alpha$ leads to higher flow adherence and lower curvature, with consistent trends in both regular and random environments.

### E. Real Urban Case Study

We select a block–scale urban area and extract building footprints and roads from OpenStreetMap [19]. The data undergoes projection to a local UTM frame and rasterization onto a uniform $120 \times 120$ grid, where $\Delta x = \Delta y$. Fig. 8(a) shows the top–down base map overlaid with the grid, and Fig. 8(b) displays the resulting binary occupancy map. Subsequently, the process groups the occupied cells into building blocks and assigns heights. The height of each block is derived from available OSM tags, yielding an extruded 3D scene with an altitude limit of 70 units.

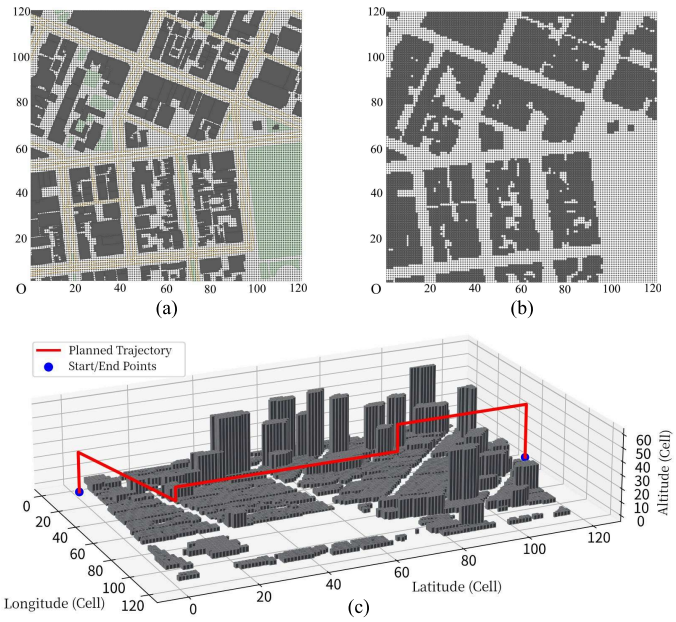


Fig. 8: Case study results in a real urban environment. (a) Top–down map of the selected block overlaid with a uniform analysis grid. (b) Rasterized building occupancy clipped to the grid and used as the input of planner. (c) Extruded 3D block model with the trajectory computed by the full model; blue dots mark the start and goal.

For a given pair of take–off and landing sites $\mathbb{T}$, the full model computes a trajectory by the A* algorithm on the 3D grid under anisotropic cost that combines traversability and flow guidance. The resulting trajectory appears in Fig. 8(c) as a red polyline. This setup aligns with the discretization and geodesic planning described in previous sections and facilitates a consistent evaluation in a realistic map context. This result confirms that the dual–field field successfully guides the planner through high–traversability regions while adhering to the macroscopic flow, producing a path that is both safe and structured.

## V. CONCLUSIONS

In this work, we have presented a novel dual–field framework that represents complex urban airspace using a coupled potential field for macroscopic traffic flow and a traversability field for continuous spatial risk. We have formulated path planning as a geodesic computation on the resulting anisotropic manifold and have integrated the model into a centralized UTM system capable of efficient, local updates. Simulation results have validated this approach: an ablation study has demonstrated that both fields are critical for generating safe and orderly paths, while a dynamic analysis has shown our local update mechanism to be significantly more efficient than global re-computation for real–time operations. Future work will focus on validating the framework on physical UAV platforms and extending it to decentralized multi–agent coordination strategies.

## REFERENCES


[1] S. S. Ahmed, G. Fountas, V. Lurkin, P. C. Anastasopoulos, Y. Zhang, M. Bierlaire, and F. Mannering, "The state of urban air mobility research: An assessment of challenges and opportunities," *IEEE Transactions on Intelligent Transportation Systems*, 2024.

[2] H. E. Tekaslan and E. M. Atkins, "Gradient guided search for aircraft contingency landing planning," in *2025 IEEE International Conference on Robotics and Automation (ICRA)*, 2025, pp. 526–532.

[3] Q. Wu, K. Liu, and L. Chen, "Model predictive control-based value estimation for efficient reinforcement learning," *IEEE Intelligent Systems*, vol. 39, no. 3, pp. 63–72, 2024.

[4] A. Moortgat-Pick, M. Schwahn, A. Adamczyk, D. A. Duecker, and S. Haddadin, "Autonomous uav mission cycling: A mobile hub approach for precise landings and continuous operations in challenging environments," in *2024 IEEE International Conference on Robotics and Automation (ICRA)*. IEEE, 2024, pp. 8450–8456.

[5] M. Aljohani, R. Mukkamala, and S. Olariu, "Delivery of medical supplies to remote locations via unmanned aerial vehicles: Approaches, challenges, and solutions," *Transportation Research Procedia*, vol. 84, pp. 73–80, 2025.

[6] P. Stockel, P. Wallrath, R. Herschel, and N. Pohl, "Detection and monitoring of people in collapsed buildings using a rotating radar on a uav," *IEEE Transactions on Radar Systems*, vol. 2, pp. 13–23, 2023.

[7] A. Marut, P. Wojciechowski, K. Wojtowicz, J. Djabin, J. Kochan, and M. Kurenda, "Surveillance and protection of critical infrastructure with unmanned aerial vehicles," in *2024 IEEE International Workshop on Technologies for Defense and Security (TechDefense)*, 2024, pp. 312–317.

[8] M. Zhang, B. Pang, C. Yan, M. Feroskhan, and C. Lv, "Real-time avoidance of obstacles and emergent geo-fences for urban air mobility using deep reinforcement learning," *IEEE Transactions on Intelligent Transportation Systems*, 2025.

[9] L. J. Prinzel, P. Krois, K. K. Ellis, M. Vincent, C. Stephens, N. Oza, E. T. Chancey, M. Davies, R. Mah, J. Ackerson *et al.*, "The adaptable and resilient safety system: The human factor in future in-time aviation safety management systems," in *AIAA SCITECH 2024 Forum*, 2024, p. 1603.

[10] P. Kopardekar, J. Rios, T. Prevot, M. Johnson, J. Jung, and J. E. Robinson, "Unmanned aircraft system traffic management (utm) concept of operations," in *AIAA Aviation Forum and Exposition*, no. ARC-E-DAA-TN32838, 2016.

[11] A. Hamissi, A. Dhraief, and L. Sliman, "A comprehensive survey on conflict detection and resolution in unmanned aircraft system traffic management," *IEEE Transactions on Intelligent Transportation Systems*, 2024.

[12] A. Li, M. Hansen, and B. Zou, "Traffic management and resource allocation for uav-based parcel delivery in low-altitude urban space," *Transportation Research Part C: Emerging Technologies*, vol. 143, p. 103808, 2022.

[13] L. Stuive and F. Gzara, "Airspace network design for urban uav traffic management with congestion," *Transportation Research Part C: Emerging Technologies*, vol. 169, p. 104882, 2024.

[14] H. Rastgoftar, H. Emadi, and E. M. Atkins, "A finite-state fixed-corridor model for uas traffic management," *IEEE Transactions on Intelligent Transportation Systems*, vol. 25, no. 3, pp. 2322–2330, 2023.

[15] N. Zheng, Y. Xu, K. Cai, and G. Inalhan, "A digital-twin based airspace corridor design and dynamic configuration for high-density uas traffic management," in *2025 Integrated Communications, Navigation and Surveillance Conference (ICNS)*. IEEE, 2025, pp. 01–11.

[16] A. El Asslouj, H. Uppaluru, M. Ramezani, E. Atkins, and H. Rastgoftar, "A fixed air corridor model for uas traffic management in urban areas," *IEEE Transactions on Aerospace and Electronic Systems*, vol. 60, no. 5, pp. 5651–5662, 2024.

[17] J. R. Sánchez-Ibáñez, C. J. Pérez-Del-Pulgar, J. Serón, and A. García-Cerezo, "Optimal path planning using a continuous anisotropic model for navigation on irregular terrains," *Intelligent Service Robotics*, vol. 16, no. 1, pp. 19–32, 2023.

[18] W. Zhang, S. Xu, P. Cai, and L. Zhu, "Agile and safe trajectory planning for quadruped navigation with motion anisotropy awareness," in *2024 IEEE/RSJ International Conference on Intelligent Robots and Systems (IROS)*. IEEE, 2024, pp. 8839–8846.

[19] M. Haklay and P. Weber, "Openstreetmap: User-generated street maps," *IEEE Pervasive computing*, vol. 7, no. 4, pp. 12–18, 2008.